International Journal of Pharmaceutics 690 (2026) 126568

Contents lists available at ScienceDirect

International Journal of Pharmaceutics

journal homepage: www.elsevier.com/locate/ijpharm

Protein delivery to the eye: assessing therapeutic potential across inner and outer retina

Giuditta Dal Cortivo [a,1], Carmen Longo [a,1], Brigitte Müller [b], Anna Avesani [a], Raffaella Pacchiana [a], Maria Weller [b], Valerio Marino [a], Lyubomyr Lytvynchuk [b], Knut Stieger [b,*], Daniele Dell'Orco [a,*]

[a] Department of Neurosciences, Biomedicine and Movement Sciences, Section of Biological Chemistry, University of Verona, Verona, Italy
[b] Department of Ophthalmology, Faculty of Medicine, Justus-Liebig-University Giessen, Germany

ARTICLE INFO

Keywords:
Protein ocular delivery
Retinal explants
Peripheral vs central retina
GCAP1
Photoreceptors
Ganglion cells
Liposomes
Ocular therapeutics

ABSTRACT

Protein-based therapeutics represent a promising approach for treating diseases of the retina, yet effective delivery systems and translational models remain limited. We developed a robust *ex vivo* framework utilizing murine and porcine retinal explants to investigate protein delivery mechanisms for both peripheral and central retinal regions. Using guanylate cyclase-activating protein-1 (GCAP1) as a retina-specific model protein and mCardinal2 as a non-retina-specific control, we demonstrated spontaneous protein internalization and accumulation in photoreceptors and ganglion cells following single-dose administration. In murine explants, myristoylated GCAP1 exhibited sustained retention and appropriate subcellular targeting in rod photoreceptors over 96 h without inducing tissue damage. Porcine explants, which better recapitulate human macular architecture, revealed differential protein trafficking dependent on post-translational modifications. Retinal tissue showed preferential uptake and retention of retina-specific proteins over foreign proteins, suggesting sophisticated protein-specific recognition mechanisms. Liposomal encapsulation enhanced initial uptake of non-retina-specific proteins but did not improve long-term retention. This experimental platform provides a valuable tool for screening protein therapeutics, optimizing delivery formulations, and investigating protein-selective cellular uptake mechanisms, with direct implications for developing treatments for inherited retinal degenerations, age-related macular degeneration, and optic nerve pathologies.

1. Introduction

Retinal diseases constitute a significant burden on society. The progressive aging and overall growth of the global population are accompanied by a rising incidence of advanced forms of age-related macular degeneration (AMD) representing the 8.7% of all blindness worldwide, affecting an estimated 196 million people globally, with projections reaching 288 million by 2040 (Wong et al., 2014), and for which therapeutic options remain limited (Singh et al., 2024). Furthermore, the incidence of severe optic neuropathies caused by glaucoma (which currently affects 3.5% of the population aged 40–80 years), ischemic and inflammatory diseases, is expected to rise (Tham et al., 2014). Additionally, inherited retinal dystrophies (IRDs) that lead to photoreceptor cell death and progressive blindness remain essentially incurable to date, with the exception of some limited cases of successful gene therapy (Hanany et al., 2024). As all these conditions often lead to irreversible loss of visual function and impaired visual adaptation, and current therapies offer only limited and often insufficient efficacy, there is a pressing need to explore alternative treatment strategies at the cellular and subcellular level.

In recent years, intraocular delivery of proteins and peptides has shown remarkable potential for the treatment of ocular diseases (Attia and MacKay, 2022; El Sanharawi et al., 2010; Mandal et al., 2018). Our previous studies have demonstrated that protein delivery to the murine retina, both *ex vivo* and *in vivo*, results in effective release into photoreceptors with proven functional effects, upon administration of the protein either in its free form or encapsulated in biocompatible lipid nanovesicles (liposomes) (Asteriti et al., 2015). Delivered proteins were

* Corresponding authors.
E-mail addresses: Knut.Stieger@uniklinikum-giessen.de (K. Stieger), daniele.dellorco@univr.it (D. Dell'Orco).
[1] These authors contributed equally and should be considered co-first authors.

https://doi.org/10.1016/j.ijpharm.2026.126568
Received 11 November 2025; Received in revised form 2 January 2026; Accepted 4 January 2026
Available online 5 January 2026

also observed in the ganglion cell layer (Asteriti et al., 2023). These studies lay the foundation for exploiting controlled protein release to the retina to treat both outer and inner retinal diseases, including those affecting the optic nerve such as glaucoma or other forms of optic atrophy. Besides protein supply and replacement, protein delivery can indeed involve the release of genome editing systems based on ribonucleoprotein complexes like Cas9-sgRNA, thus constituting promising tools for ultimate IRDs' therapy (Karp et al., 2025). To formulate targeted therapeutic hypotheses, adequate experimental models with high translational potential are required, enabling direct assessment of biocompatibility and low immunogenicity of therapeutic molecules. The successful administration of candidate biological drugs, following formulation and pharmacokinetic refinement, strongly depends on the availability of a controlled system to characterize their biodistribution and time course across retinal layers.

In this work, based on robust culture methods for murine (Muller, 2019) and porcine retinal explants (Weller et al., 2024), we present a novel framework for investigating the potential of protein delivery to the human retina, using systems that suitably mimic release in both peripheral and central retinal regions. We sought to address fundamental questions relevant to the translational application of protein delivery such as i) the precise localization of the delivered protein across retina layers; ii) the role of post-translational modifications in protein biodistribution; iii) the safety of protein delivery; iv) the distinction between the delivery of retina-specific vs non-retina-specific proteins. As a model system, we used the endogenous protein guanylate cyclase-activating protein-1 (GCAP1), which acts as a neuronal calcium sensor switching between Mg^{2+}-bound and Ca^{2+}-bound forms (Marino et al., 2015) necessary to activate and deactivate the target enzyme guanylate cyclase 1, respectively (Koch and Dell'orco, 2013, 2015). GCAP1 is therefore an essential regulator of the phototransduction cascade in vertebrates (Koch and Dell'Orco, 2015), whose mutations are implicated in various retinal dystrophies, including cone and cone-rod dystrophies (Biasi et al., 2021; Dell'Orco et al., 2010; Dizhoor et al., 1998; Jiang et al., 2008; Kamenarova et al., 2013; Kitiratschky et al., 2009; Manes et al., 2017; Marino et al., 2021; Marino et al., 2018; Nishiguchi et al., 2004; Peshenko et al., 2019; Sokal et al., 2005; Sokal et al., 1998; Vocke et al., 2017; Wilkie et al., 2001), as well as retinitis pigmentosa (Abbas et al., 2020), thereby providing our findings with valuable therapeutic implications. We compare the internalization of the retina-specific GCAP1 protein with the non-retina-specific protein mCardinal2 to assess potential recognition mechanisms of the delivered proteins operating in the retina.

The dual targeting capability of our system demonstrates protein accumulation in both photoreceptor and ganglion cell layers. The therapeutic potential of our approach is broadened by its possible application in elucidating molecular mechanisms leading to or preventing the degeneration of retinal layers, with focus on the macula threatening diseases (including AMD and IRDs), or ganglion cells, with important implications for glaucoma and optic neuropathies of different origin.

2. Materials and methods

2.1. Materials

The following materials were purchased from Merck (Darmstadt, Germany): tris(hydroxymethyl)aminomethane (Tris), guanidine-HCl, potassium chloride (KCl), sodium chloride (NaCl), calcium chloride dihydrate ($CaCl_2$), magnesium chloride ($MgCl_2$), 3-(N-morpholino)propanesulfonic acid (MOPS), dithiothreitol (DTT), ethylene glycol-bis (β-aminoethyl ether)-N,N,N′,N′-tetraacetic acid (EGTA), ethylenediaminetetraacetic acid (EDTA), β-mercaptoethanol, ammonium bicarbonate (NH_4HCO_3), 4-(2-hydroxyethyl)-1-piperazineethanesulfonic acid) (HEPES), myristic acid, ampicillin (Amp), kanamycin (Kan), isopropil-β-D-tiogalattopiranoside (IPTG), lysozyme, phosphatidylcholine (PC), phosphatidylserine (PS), phosphatidylethanolamine (PE), α-tocopherol (α-toc), cholesterol (Ch), acrylamide bis-acrylamide, coomassie blue, acetonitrile (ACN), trifluoroacetic acid (TFA), paraformaldehyde (PFA), formalin, sucrose, Optimal Cutting Temperature medium (OCT), ammonium chloride (NH_4Cl), Triton X-100, Tween20, bovine serum albumin (BSA), cOmplete EDTA-free protease inhibitor cocktail (PIC), adenosine triphosphate (ATP), guanosine triphosphate (GTP), Zaprinast, cyclic guanosine monophosphate (cGMP), methanol (MetOH), gelatine, chromium(III) potassium sulfate dodecahydrate, hydrogen peroxide, inserts with a polycarbonate membrane, 0.4 μm pore size (BR782740) used for explants culturing, and C18-RP HPLC column (LiChrosphere® 100 5 μm). His-trap FF crude column and Sephacryl S-100 HR column were purchased from Cytiva.

Luria Bertani broth (LB), DNAse I, Dulbecco's modified eagle medium (DMEM), penicillin, streptomycin, 2-(4-amidinophenyl)-1H-indole-6-carboxamidine (DAPI), Phosphate Saline Buffer (PBS), fetal bovine serum (FBS), Hanks' balanced salt solution (HBSS), glutamine, normal goat serum (NGS), normal donkey serum (NDS), Neurobasal no glucose and high glucose, Roswell Park Memorial Institute 1640 Medium (RPMI 1640), B27 and N2 supplements, antibiotic-antimycotic (anti-anti), were purchased from ThermoFisher Scientific (Waltham, MA, USA).

Fluorescence mounting medium (Agilent Dako, Santa Clara, CA) was used for glass slides mounting, all the primary, secondary antibodies and fluorescent probes used, their dilutions and manufacturers are listed in Table 1.

2.1.1. Animal procedures

All animal procedures were performed in accordance with Italian Governing law (D.lgs 26/ 2014; Authorization n.19/2008-A issued March 6, 2008, by Ministry of Health); the NIH Guide for the Care and Use of Laboratory Animals (2011edition) and EU directives and guidelines (EEC Council Directive 2010/63/UE). The experiments have been performed in compliance with the ARRIVE guidelines.

C57-BL6J mice were housed under standard environmental conditions (controlled temperature and humidity) with *ad libitum* access to food and water and maintained on a 12-hour light/dark cycle.

2.2. Methods

2.2.1. Expression and purification of human GCAP1-His

Human GCAP1 cDNA was cloned in a pET11a(+) plasmid carrying a 6xHis-tag at the C-term by Genscript. Protein myristoylation, which occurs at the N-terminus on the glycine residue, was obtained as detailed previously (Marino et al., 2018) and explained here briefly. *E. coli* BL21 DE3 cells were co-transformed using pET11a(+) and pBB131 plasmids, encoding for human GCAP1-His and yeast N-myristoyl-transferase respectively. Cells were grown in LB-broth in the presence of both Amp (100 μg/mL) and Kan (30 μg/mL) until the OD_{600} reached 0.4, then myristic acid was added to obtain a final concentration of 50 μg/mL.

Table 1
Primary and secondary antibodies used for immunofluorescence detection.

Antigen	Product code	Manufacturer	Dilution
GCAP1 (rabbit)	Kind gift by Jeannie Chen; see (Lopez-Begines et al., 2018)	homemade	1:200
GFAP (rabbit)	AB5804	Millipore	1:1000
GRK1 (rabbit)	A6497	AbClonal	1:200
His-tag (mouse)	4603-01M	SouthernBiotech	1:600
PNA	L-21409	Molecular Probes	1:50
Phalloidin 647	A30107	Invitrogen	1:1000
AlexaFluor anti-mouse 647	A21235	Invitrogen	1:1000
AlexaFluor anti-rabbit 568	A-10042	Invitrogen	1:1000
DAPI	Invitrogen	Invitrogen	1:1000

Protein expression was induced adding 1 mM IPTG at $OD_{600} = 0.6–0.7$. The non-myristoylated GCAP1-His was obtained growing cells missing the pBB131 plasmid and avoiding the addition of myristic acid. Both myristoylated and non-myristoylated forms were purified using a combination of Size Exclusion Chromatography and Anionic Exchange Chromatography, as elucidated by Marino et al. (2018), and protein purity was assessed by Sodium Dodecyl Sulphate-PolyAcrylamide Gel Electrophoresis (SDS-PAGE). The myristoylation yield was evaluated using a High-Performance Liquid Chromatography based method. Briefly, a C18-Reverse Phase column (Lichrosphere®) maintained at room temperature was equilibrated using bi-distilled water +0.1% TFA (solvent A). Protein samples in PBS were injected at a volume of 50 µL (concentration 0.5–1 µg/µL) for both i) non-myristoylated GCAP1-His (as a negative control) and ii) myristoylated GCAP1-His. A 55 min linear gradient from 0% to 100% ACN + 0.1% TFA (solvent B) was applied at a flow rate of 0.5 mL/min, with detection at 280 nm. The presence of the myristoyl moiety covalently bound at the N-terminus increased protein hydrophobicity, resulting in delayed protein elution at higher organic solvent concentrations compared to the negative control. The myristoylation efficiency was estimated by comparing the peak areas in the chromatograms: nmGCAP1-His eluted as a single peak at ~70% of the gradient, while mGCAP1-His showed two peaks – one co-eluting with the non-myristoylated form (representing residual nmGCAP1-His) and a second, more abundant peak eluting at a later retention time (see Fig. S1 for a representative chromatogram). The myristoylation percentage was calculated as follows:

$$\%Myristoylation = \frac{Area_{myr\_peak}}{Area_{myr\_peak} + Area_{nonmyr\_peak}} * 100$$

A myristoylation efficiency >90% was detected. Finally, the purified proteins were dialyzed against 50 mM ammonium bicarbonate, lyophilized and stored at −80 °C until use.

2.2.2. mCardinal2 expression and purification

Plasmid pNCS-mCardinal2 (Addgene #52631) was used to transform DH5α *E. coli* strain for the expression of histidine-tagged mCardinal2 (mCar2-His). Briefly, one colony of transformed cells was pre-inoculated in 10 mL of sterile LB-broth supplemented with Amp (100 µg/mL) and cultured overnight at 37 °C, 180 rpm. The overnight pre-culture was inoculated in 750 mL of sterile LB-broth/Amp. After 20 h incubation at 37 °C and 180 rpm, cells were harvested and the pellet resuspended in 20 mL of 50 mM Tris-HCl pH 7.4, 150 mM NaCl, 0.1 mg/mL lysozyme, 5 U/mL DNAse I, protease inhibitors cocktail and kept on ice 30 min. Cell lysate was then sonicated for 15 min on ice setting 2 sec on and 3 sec off cycles using a Pulse 150 Ultrasonic Homogenizerand, after centrifugation at 18000 rpm, 30 min, 4 °C the supernatant was filtered through 0.45 µm CA membrane and loaded on HisTrap FF crude column and eluted with 300 mM imidazole in 50 mM Tris-HCl pH 7.4, 150 mM NaCl. The fractions corresponding to mCar2-His were further purified by size exclusion chromatography using a Sephacryl S-100 HR column equilibrated with phosphate buffer saline (PBS) pH 7.4. After assessing purity grade by SDS-PAGE, protein was shock frozen in liquid nitrogen and stored at −20 °C, final yield 135 mg/L.

2.2.3. Biochemical and biophysical characterization of delivered proteins

To check whether the presence of the His-tag at the C-term of GCAP1-His affects or not its capability to respond to ions, circular dichroism (CD) spectra were collected using a Jasco J-710 spectropolarimeter equipped with a Peltier-type cell holder. Lyophilized myristoylated (mGCAP1-His) and non-myristoylated GCAP1 (nmGCAP1-His) were resuspended in 0.1 M PBS pH 7.4 at a final concentration of 12 µM for far-UV (200–250 nm) and 24–28 µM for near-UV (230–320 nm) CD spectroscopy, collecting spectra after sequential additions of 500 µM EDTA, 1.5 mM Mg^{2+} and 500 µM Ca^{2+}. Temperature was set at 37 °C, time response at 4 sec and data pitch at 1 nm. The obtained spectra represent an average of 5 accumulations, and the spectrum of the sole PBS was considered as blank and subtracted.

For biophysical characterization of mCar2-His, the protein was prepared in 20 mM Tris-HCl pH 7.5, 150 mM KCl at a final concentration of 12 µM for far-UV CD spectroscopy (200–250 nm) and 43 µM for near-UV/Vis CD spectroscopy (250–700 nm). Spectra were recorded at 25 °C with 3 (near UV CD) or 5 (far UV CD) accumulations. UV–Vis spectra of mCar2-His were recorded in the range 250–700 nm using 13.5 µM protein in PBS pH 7.4 at 25 °C using a Jasco spectrophotometer V-650. Fluorescent spectra of mCar2-His were collected at 25 °C in the range 620–750 nm using 12.5 µM protein in PBS pH 7.4 using $\lambda_{Ex} = 603$ nm using a Jasco spectrofluorimeter FP-8500.

To assess the proteins purity and the Ca^{2+}-binding properties of mGCAP1-His and nmGCAP1-His, a gel shift assay was performed as described in (Marino et al., 2018). Briefly, 15 µM GCAP1-His variants were incubated in the presence of 0.5 mM EDTA, 0.5 mM EGTA + 1.1 mM Mg^{2+} or 1 mM Mg^{2+} + 0.5 mM Ca^{2+} for 10 min at RT. Then, after the addition of reducing sample buffer, samples were boiled at 96 °C for 5 min, loaded into a 15% SDS-PAGE, run for 40–45 min at 200 V (constant) and finally Coomassie blue stained.

2.2.4. Guanylate cyclase assay

To validate the functional properties of recombinant m- and nmGCAP1-His we directly tested their capability to regulate the catalytic activity of the target enzyme (Guanylate Cyclase 1). The full protocol is well described in (Marino et al., 2018) and summarized as follows: 5 µM GCAP1-His variants were incubated for 5 min at 30 °C with membranes from a stable cell line expressing GC1-GFP in the absence (< 20 nM) or presence of saturating Ca^{2+} (30 µM) using K_2H_2EGTA – $K_2CaEGTA$ buffers. Reactions stopped adding 0.1 M EDTA and incubating the mixture for 5 min at 96 °C. Finally, samples were centrifuged at 16000 rpm to get rid of denatured protein and membranes, and the obtained supernatant loaded onto a C18-RP HPLC column for the cGMP quantification.

2.2.5. Liposome preparation

Liposomes were prepared using the lipid film hydration approach. Briefly, a 2 mg mixture of lipids mimicking the composition of photoreceptors rod outer segments membrane (PE, PC, PS, Ch and α-toc at a molar ratio of 35:35:15:5:10) was hydrated with 1 ml of 162 µM mCar2-His in PBS at pH 7.4, vortexed for 15 min at room temperature, sonicated 15 min on ice in a water bath and underwent 20 extrusion passages through a 100 nm diameter polycarbonate membrane (Whatman, Maidstone, UK). The liposome suspension was washed twice with PBS pH 7.4 via centrifugation for 5 min at 5000×g in an Amicon concentrator with 100 kDa cutoff (Merck Millipore, Burlington, MA, USA) to remove unencapsulated mCar2-His. The encapsulation efficiency was evaluated by measuring the mass of the protein in the flow-through of the two washing steps (ε at 280 nm = 25600 M^{-1} cm^{-1}) and subtracting it from the mass of protein used to hydrate the lipid film and was found to be >75%. The concentration of the unencapsulated protein present in the final liposome suspension was estimated from the flow-through of second washing step and was found to be <5% of the total encapsulated protein.

2.2.6. Nanoparticle tracking analysis (NTA)

Liposome size and concentration were measured by NTA on a NanoSight instrument (Malvern Instruments, Malvern, UK). Briefly, 3 one-minute videos at 25 fps of a 1:10000 dilution of liposomes in water were collected at 20 µl/min flow rate, detection threshold and camera level were auto- adjusted by the software to increase the signal-to-noise ratio. Liposome's size reported in Fig. 1F is the mode ± standard deviation of 3 technical replicates.

2.2.7. Dynamic light scattering (DLS)

Liposome hydrodynamic diameter was also estimated via DLS on a Zetasizer Nano-S (Malvern Instruments, Malvern, UK). Briefly, a 1:10

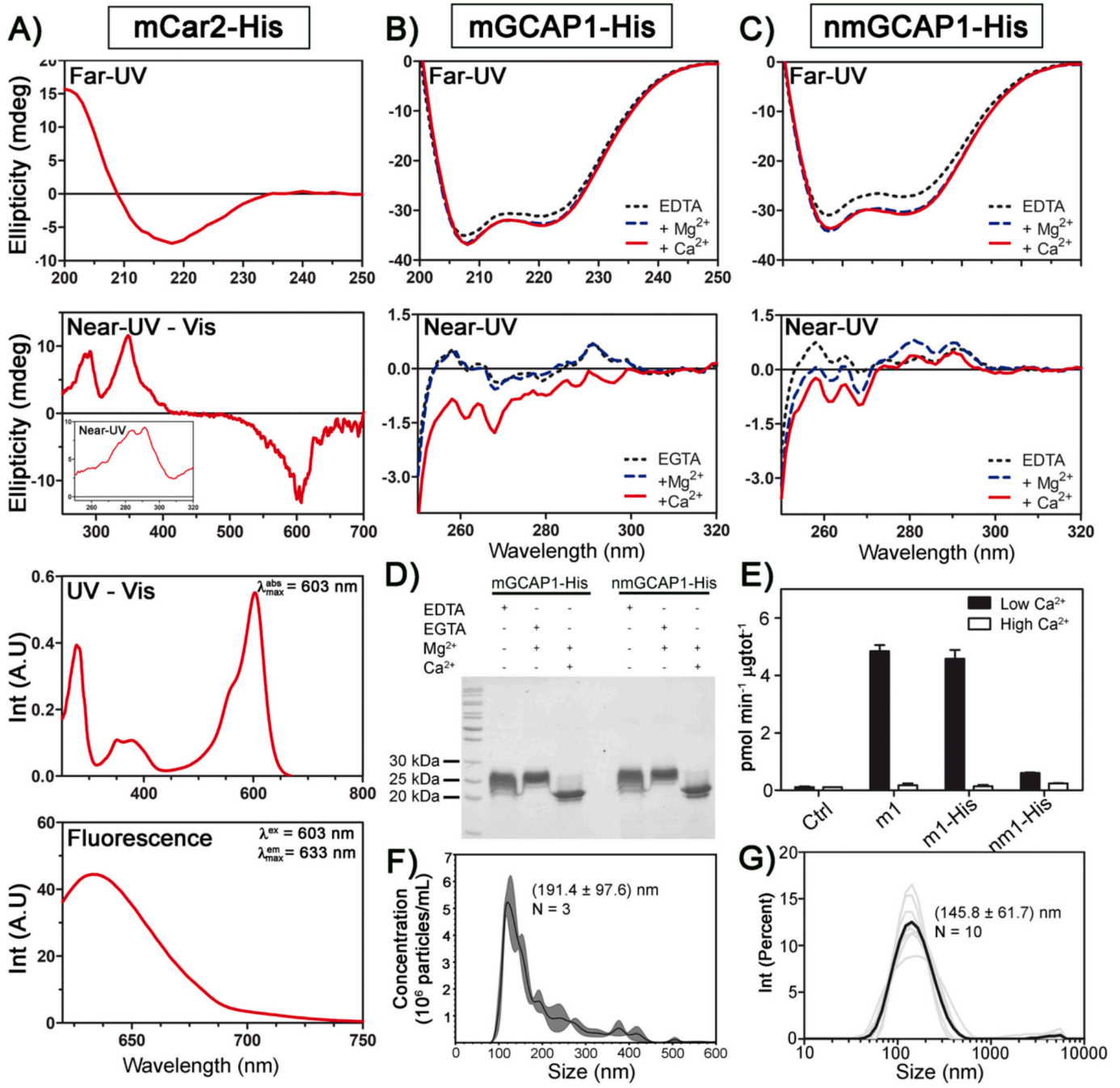

Fig. 1. Biophysical and biochemical characterization of recombinant proteins used as probes. A) mCar2-His spectra collected via circular dichroism at 42.6 μM (near-UV–Vis, 250–700 nm, 1 cm path length) and 11.8 μM (far-UV, 200–250 nm, 1 mm path length); UV–Vis (13.5 μM, 250–700 nm); and fluorescence spectroscopy 12.5 μM, λ_{Ex} = 603 nm, λ_{Em} = 620–750 nm) to assess protein structure and fluorescence properties B-C) CD spectra of mGCAP1-His (B) and nmGCAP1-His (C) were recorded at 20 μM (near-UV, 320–250 nm, 1 cm path length) and 12 μM (far-UV, 200–250 nm, 1 mm path length). Measurements were performed under three conditions: apo (0.5 mM EDTA), after addition of 1 mM free Mg^{2+}, and following supplementation with 0.5 mM free Ca^{2+}. Spectra represent the average of five accumulations and were acquired at 37 °C with a 4 s time response. The spectrum of sole 0.1 M PBS pH 7.4 was considered as blank and subtracted. D) Gel-shift assays were carried out with 15 μM GCAP1-His variants under the following conditions: (i) 0.5 mM EDTA, (ii) 1 mM EGTA + 1.1 mM Mg^{2+}, and (iii) 1 mM Mg^{2+} + 0.5 mM Ca^{2+}. Samples were incubated for 10 min at room temperature, mixed with 4× loading buffer, heated at 95 °C for 5 min, resolved by 15% SDS–PAGE, and visualized by Coomassie Blue staining. E) Guanylate cyclase 1 activity was assessed with 5 μM GCAP1-His variants in the presence of low (<20 nM) or high (30 μM) Ca^{2+}. m1 stands for mGCAP1 without the His-tag, m1- and nm1-His stands for the His-tag variants. Further methodological details are provided in the Methods section. F-G) Liposomes carrying mCar2-His as cargo were assessed via NTA (F) and DLS (G) with the aim of measuring colloidal properties. The value reported on (F) represents the mode ± SD, while in (G) is the average ± SD.

dilution of liposome suspension in PBS was loaded on a low volume disposable cuvette polystyrene and after 1 min equilibration at 25 °C, 10 measurements (each consisting of 13 runs) were recorded with the following parameters: Refractive index = 1.332, viscosity = 0.9233 cP, measurement angle = 173° backscatter, analysis model = multiple narrow modes. Liposome diameter reported in Fig. 1G is the average ± standard deviation of 10 technical replicates.

2.2.8. Adult mouse retina explants

Explants from adult C57-BL6J mice were prepared as described in (Muller, 2019; Muller et al., 2017). To avoid confounding effects from retinal maturation or aging, adult mice (P90–P100, males and females equally represented) were used. Following mouse euthanasia via cervical dislocation, eyeballs were enucleated and briefly rinsed in 70% ethanol and 1X HBSS. Eyecups were obtained by sectioning at the *ora serrata* and removing the lens. Retinal explants were prepared in two configurations to assess aging dynamics: whole retinas and quarters. For whole explants, four radial incisions were performed to generate a cloverleaf shape, whereas for quarters the incisions were completed with a scalpel. Tissue fragments were transferred into culture inserts with photoreceptors oriented toward the insert membrane and incubated at 37 °C for 1 h in DMEM++- (DMEM supplemented with 2 mM glutamine and 1X penicillin–streptomycin). The medium was then replaced with DMEM++++ (DMEM++- further supplemented with 25% 1X HBSS and 25% FBS). Explants were maintained at 37 °C, 5% CO_2, with medium renewal every other day using DMEM++++. Retinal quarters were treated with recombinant mGCAP1-His. Unlike previous experiments performed in (Asteriti et al., 2023), where large protein amounts were applied without precise tissue orientation, here we aimed to approximate a pharmacologically feasible dose. Based on geometric approximations and literature data, we estimated that a rod photoreceptor contains ~5 fg of GCAP1 and, given that a mouse retina comprises ~6.4 million rods, the total endogenous GCAP1 content per retina was calculated to be ~32 ng (Fu and Yau, 2007; Hwang et al., 2003; Jeon et al., 1998). Considering detection limits of the available instrumentation, treatments were performed on retinal quarters, considered as experimental units (ARRIVE 1b), by administering a single dose of 430 ng recombinant protein (approximately 50-fold the endogenous level) to 1-day explants.

Tissues were collected at 24 h, 48 h, 72 h, and 96 h post-treatment, with time-matched negative controls processed in parallel, in accordance with ARRIVE 1a. Three technical replicas were prepared for each tested condition (ARRIVE 2a), tissues came from left or right eyes of different animals, independently of their gender. For harvesting, tissues were fixed for 40 min in 4% PFA and after three washes in 0.1 M PBS (pH 7.4), they were subjected to a sucrose gradient cryoprotection protocol: 15 min in 10% sucrose, 15 min in 20% sucrose, and 1 h in 30% sucrose at RT, followed by overnight incubation at 4 °C. The following day, samples were incubated for 1 h at RT in a 1:1 mixture of 30% sucrose and OCT (cryogenic embedding medium), then gradually frozen in liquid nitrogen (avoiding direct contact) and stored at −80 °C until further processing. Sagittal sections were prepared by cutting tissues in a cryostat (Leica) setting the temperature at −14 °C and the thickness at 14 µm. Sections were moved on glass slides previously treated with Cromalin solution (0.5% gelatin, 0.1% Chromium(III) potassium sulfate dodecahydrate) and stored at −80 °C until usage.

2.2.9. Pig retinal explants

Pig explants were prepared as described in (Weller et al., 2024). Porcine eyes were obtained from a local butcher immediately after sacrifice and were placed in a bottle of ice-cold transport buffer (40% DMEM high glucose (−) Glutamine, 40% RPMI 1640, 10% HEPES 250 mM, and 10% anti-anti) and kept on ice until they were processed. Eyes coming from adult pigs, males and females equally represented, were processed within 3 h after enucleation. Dissection was performed under a laminar flow hood. Excessive tissue was removed from intact eyes, then eyeballs were washed in 70% ethanol and rinsed with MilliQ H_2O. Cornea, lens, and vitreous were removed with the help of scalpel and scissors; pig eyecup was kept hydrated with PBS. The periphery was then eliminated, and the remaining visual streak was cut into 3–4 square pieces with a 3- to 4-mm edge length, considered as the experimental unit. The retina was carefully peeled from the underlying RPE with the help of a raspatorium/freer elevator OL165r and placed in a drop of culture medium (20.2% Neurobasal A medium high glucose (−) Glutamine, 70.8% Neurobasal A medium no glucose, 2% B27 with insulin, 1% L-Glutamine, 5% anti-anti, 1% N-2 supplement) on the semi-permeable membrane insert (polycarbonate, 0.4 µm pore size) in a six-well format with the photoreceptors facing the membrane. Any excess of medium was carefully removed around the explant with a pipette and 1.2 mL culture medium were added to each well under the membrane insert. Three treatments were tested on three experimental units: i) ~60 µg of free mCar2-His, ii) ~44 µg of GCAP1-His variants or iii) liposomes loaded with a total amount of mCar2-His identical to that used in the free-protein conditions. A volume of 20 µL of each treatment was administered once directly pipetted on the explants (nothing on the negative control), which were cultured in sterile incubator at 37 °C, 5% CO_2. Explants were harvested at day 1 and 7 after treatment and processed as follows: after 1 h in 10% formalin and 3 x 15 min wash in 0.1 M PBS pH 7.4, a sucrose gradient was performed (2 h 10%, 2 h 20%, 1 h 30% at room temperature) and the explants were stored overnight in 30% sucrose at 4 °C. The day after, sucrose was replaced with 30% sucrose:OCT 1:1, kept at RT for 1 h before freezing in liquid nitrogen as for mouse explants. Fourteen micrometer retinal cross sections were cut at T = −17 °C (Leica cryostat), then moved on glass slides previously treated with Cromalin solution (0.5% gelatin, 0.1% Chromium(III) potassium sulfate dodecahydrate) and stored at −80 °C until usage.

2.2.10. Immunofluorescence

Immunofluorescence from mouse explants were performed using the Antibody Signal Enhancing protocol described by (Rosas-Arellano et al., 2016). After thawing the frozen slices for 30 min at RT, three washes using 0.1 M PBS, 0.5% Tween20 (PBS-T) were performed. Blocking solution was prepared in 0.1 M PBS pH 7.4 including 50 mM glycine, 0.05% Tween20, 0.1% Triton X-100, 0.1% BSA and 2% serum, and they were incubated for 1 h at RT, in a wet chamber in the dark. Primary antibodies were diluted as described in Table 1 using the Antibody Signal Enhancer solution (10 mM glycine, 0.05% tween20, 0.1% Triton X-100, 0.1% hydrogen peroxide prepared in 0.1 M PBS pH 7.4) and incubated ON, at 4 °C in a wet chamber. After three washes using PBS-T, samples were incubated with secondary antibodies conjugated with fluorophores (Table 1) for 1 h at RT in a wet chamber in the dark. Finally, the tissues were counterstained using DAPI and/or Phalloidin according to the manufacturers and mounted using Fluorescence Mounting Medium.

Immunostaining on pig explants were performed as follows: after having dried the slides for 30 min at RT, they were washed in 0.1 M PBS three times and blocked using 5% bovine serum albumin and 0.5% Triton X-100 in 0.1 M PBS for 1 h. After a quick rinse with PBS, tissues were incubated with primary antibodies diluted in blocking solution, ON at 4 °C in a wet chamber. The next day, after washing with PBS, secondary antibodies were incubated for 1.5 h in the dark at room temperature and then tissues were counterstained with DAPI for 5 min, rinsed with PBS, and finally covered with Fluorescence Mounting Medium. The information about primary and secondary antibodies used for immunofluorescence assay is reported in Table 1. Glass-slides were stored for a short time at 4 °C and analyzed using Evident FV4000 (Olympus) confocal microscope at 60× magnification (1.4 NA) oil immersion and 20x air objective (0.8 NA).

2.2.11. Image processing

The confocal micrographs collected were analyzed using Scientific Volume Imaging software (10.10 version, Hilversum, NL) with the following parameters: deconvolution algorithm, Classic Maximum Likelihood Estimation (CMLE); maximum iterations, 100; SNR, 20 and quality threshold, 0.05.

All images were then analyzed using Imaris software (v 10.2.0, Oxford Instruments, Belfast, UK): the colocalization analysis was performed using a Coloc tool with a defined threshold for each analyzed channel. The panels composing the figures were prepared using ImageJ software (v 1.53 t, NIH Image, Bethesda, MD, USA).

2.2.12. Statistics

All experiments involving animal tissues were performed at least in triplicates (ARRIVE 7a). Each treatment and formulation were administered to tissues obtained from different animals (biological replicates) to minimize potential variability arising from intrinsic inter-animal differences. Additionally, all staining procedures were performed in triplicates (technical replicates) to ensure reproducibility and avoid misinterpretation due to tissue-specific characteristics. Two to four micrographs per sample were acquired using confocal microscopy. Statistical analyses were performed using GraphPad Prism software. Specifically, two-tailed t-tests were conducted with statistical significance set at $p < 0.05$.

3. Results

3.1. Protein and liposome characterization for retinal delivery experiments

Intraretinal delivery experiments were conducted using two recombinant proteins prepared specifically for this purpose. A variant of human recombinant GCAP1 utilized in previous studies (Asteriti et al., 2023; Marino et al., 2018) was modified with a C-term histidine tag (GCAP1-His) to enable intracellular tracking through immunofluorescence and distinction from the endogenous protein. This protein served as proof of concept for delivery of a tissue-specific retinal protein responsible for precise biological functions. GCAP1-His was produced in both its myristoylated and non-myristoylated forms (mGCAP1-His and nmGCAP1-His, respectively), to assess the potential role of the myristoyl moiety in retina uptake and biodistribution.

The small fluorescent protein mCardinal2 incorporating the same histidine tag (mCar2-His) was also produced (Kim et al., 2022), to investigate the effect of delivering a protein with similar molecular weight (31.2 kDa), but not being retina-specific. Prior to experimental delivery, comprehensive spectroscopic and functional characterization of mCar2-His and both GCAP1-His variants were performed to ensure that protein misfolding or His-tag-related functional anomalies would not affect the results. Circular dichroism (CD) spectroscopy in the far- and near-UV regions confirmed the proper folding of both mCar2-His (Fig. 1A) and m/nmGCAP1-His variants (Fig. 1B–C). In particular, the far-UV CD spectrum of mCar2-His was consistent with that of a β-sheet-rich beta-barrel protein showing typical minima around ~216–218 nm, while the absorption maximum at 603 nm and the fluorescence emission peak around 630 nm suggested that the Methionine–Tyrosine–Glycine chromogenic tripeptide was fully functionally encased in the beta-barrel secondary structure. This was confirmed by the near-UV–Vis CD spectrum, which displayed a structured microenvironment of all aromatic residues, in particular in the Tryptophan region (280–295 nm) where an intense, positive band was detected (Fig. 1A, inset). The His-tag therefore did not compromise the folding and the fluorescence emission of mCar2-His under the conditions employed in the delivery experiments.

As to GCAP1-His, both variants demonstrated responsiveness to Mg^{2+} and Ca^{2+} binding, with subtle but significant differences in their conformational transitions (Fig. 1B-C). The transition from the apo to cation-bound state resulted in increased dichroic signal intensity, consistent with increased secondary structure and acquisition of more compact tertiary structure. This structural response was more pronounced in nmGCAP1-His compared to the myristoylated variant, as previously observed with the bovine ortholog (Dell'Orco et al., 2010). The microenvironment of aromatic residues was probed by near-UV CD analysis, which corroborated the far-UV findings. Notably, nmGCAP1-His exhibited enhanced Mg^{2+} responsiveness relative to the myristoylated form, while mGCAP1-His displayed a distinct Ca^{2+}-dependent spectral signature characterized by negative ellipticity extending into the tryptophan absorption region. These observations collectively demonstrate structural integrity and functional responsiveness of the purified proteins. Ca^{2+}-binding capacity was assessed using gel-shift assays (Fig. 1D), valuable to directly assess alterations in Ca^{2+} coordination by high-affinity calcium sensor proteins which typically show an apparent molecular weight shift to values lower than the theoretical mass upon Ca^{2+} binding (Viviano et al., 2016). This simple but informative assay was successfully used previously for other GCAP1 variants (Dal Cortivo et al., 2020; Marino et al., 2018). In the apo state, both variants exhibited a typically smeared band despite EDTA treatment, consistent with the persistence of high-affinity Ca^{2+}-binding sites of GCAP1. Mg^{2+} addition resulted in homogeneous, compact bands at the theoretical molecular weight (25 kDa), while Ca^{2+} binding induced migration to approximately 20 kDa, confirming expected conformational changes indicative of functional Ca^{2+} coordination. Finally, the potential impact of the C-terminal His-tag on guanylate cyclase 1 regulation was evaluated. Functional assessment (Fig. 1E) demonstrated that the C-terminal His-tag did not compromise the catalytic regulation of the enzyme under conditions mimicking dark/light adapted photoreceptors; the regulatory profiles of mGCAP1 and mGCAP1-His were indeed highly similar, validating the use of tagged variants. The N-terminal myristoyl group enhanced regulatory efficiency, as evidenced by superior performance of the myristoylated form compared to the non-myristoylated variant, which was already observed in the bovine ortholog (Hwang and Koch, 2002). Collectively, these biochemical and functional analyses confirm that, despite the presence of the C-terminal histidine tag, both GCAP1-His variants retain structural integrity and biological activity comparable to the untagged wild-type proteins. These results validate the use of GCAP1-His as a reliable molecular probe for protein delivery studies, ensuring that observed cellular responses reflect genuine protein uptake rather than artifacts arising from misfolded or functionally compromised variants.

We previously demonstrated that mGCAP1 can enter the murine retina regardless of being encapsulated or not in liposomes formulated to mimic the lipid composition of photoreceptor membranes. However, liposomal encapsulation was required for the protein to be internalized by cultured eukaryotic cells (Asteriti et al., 2023). To deliver the exogenous protein mCar2-His, we encapsulated it in the same type of liposomes (see Methods) and compared its delivery efficiency with that of the free protein. Liposomes exhibited high encapsulation efficiency (>75%), and a monodisperse size distribution, as assessed by both nanoparticle tracking analysis (NTA) and dynamic light scattering (DLS) (see Fig. 1F and G, respectively). The measured hydrodynamic diameter, ranging from 120 to 140 nm, was comparable to that previously observed for mGCAP1-loaded liposomes (~150 nm; see (Asteriti et al., 2023)).

3.2. Murine retina explants as a model of peripheral retina for testing protein delivery

Adult murine retinal explants (P90-100) were prepared according to established protocols (Muller et al., 2017; Weller et al., 2024). To optimize experimental design while adhering to reduction principles (3Rs), we evaluated whether retina quarters could substitute for whole retinas without compromising data quality. Both formats were maintained in culture for 120 h and assessed for glial fibrillary acidic protein (GFAP) expression as an indicator of tissue stress following a single treatment with mGCAP1-His (430 ng/explant). It is well established (Muller et al., 2017) that GFAP expression, mainly in astrocytes, increases with culturing time, and that the associated processes extend across retinal layers. We therefore treated the retinas with mGCAP1-His and monitored the cultures for up to 96 h after treatment administration (see Method for details).

GFAP immunofluorescence increased progressively in both whole retinas (Fig. S2A) and quarters (Fig. S2B), with astrocytic processes extending across retinal layers (see arrows). Quantitative analysis of maximum fluorescence intensity (Fig. S2C) revealed no significant differences between formats, validating the use of retinal quarters for subsequent experiments while minimizing animal use.

To perform protein delivery and localization studies, a pharmacologically relevant approach was adopted, employing oriented explants on membrane inserts to simulate intravitreal administration, differing from previous work from some of us, where a whole retina setup without specific orientation was used to demonstrate the uptake of high amounts (~600 μg) of mGCAP1 in both photoreceptor and ganglion cell layers (Asteriti et al., 2023). Based on estimates of endogenous GCAP1 content (~32 ng per retina, ~8 ng per quarter) (Fu and Yau, 2007; Hwang et al., 2003; Jeon et al., 1998), 430 ng of mGCAP1-His were administered as a single dose to the surface facing the ganglion cell layer. Controls tissues

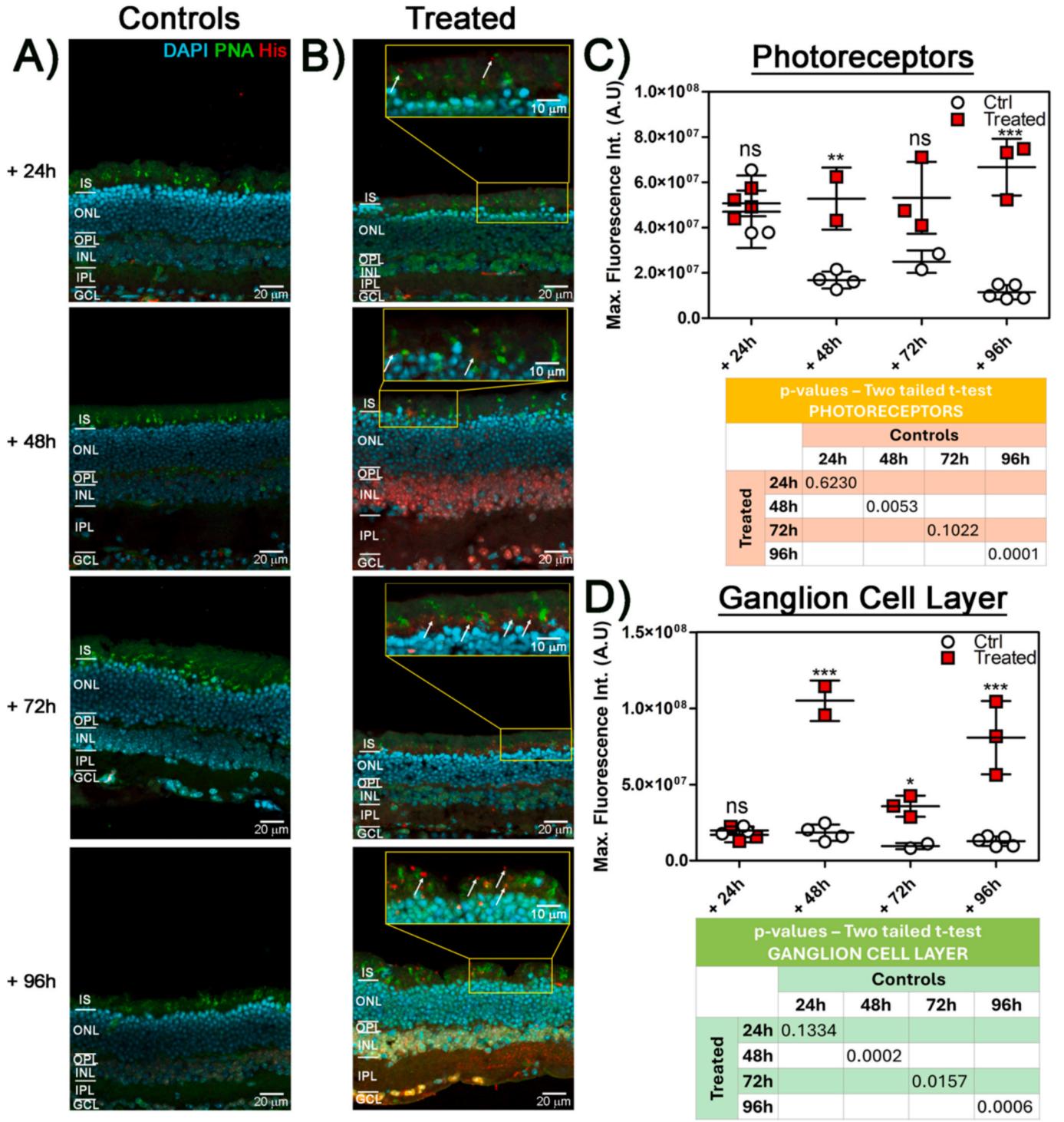

Fig. 2. Treatment accumulation in adult mouse retina explants. A-B) After the administration of a single dose of mGCAP1-His on explants ad day 1 (430 ng/explant) tissues were harvested after 24 h, 48 h, 72 h, and 96 h (B). Time-matched controls were prepared (A). Cryosections were immunostained with PNA (green), anti–His-tag primary antibody (red) and counterstained with DAPI (cyan). Representative images show maximum intensity projections (MIP) of five optical sections acquired with a z-step size of 0.9 μm using a 20× air objective (0.8 NA) with an additional 2× digital zoom (final magnification, 40×). C-D) Quantitative analysis was performed using CellSense software on photoreceptor (C) and ganglion cell layers (D), using manually defined polygonal ROIs, considering the whole z-volume. Signal intensity from the 647 channel was measured. Each circle or square represents one analyzed image. Paired two tailed t-tests were used to compare treated (red squares) and controls (white circles) at the same time point; p-values are reported in the tables.

(Figs. 2A and S3A) exhibited positive staining in the inner nuclear layer (INL) but not in the Ganglion Cell Layer (GCL) or in the outer nuclear layer (ONL), and this could be attributed to histone exposure during DNA condensation (Chilumuri et al., 2014). Treated tissues, on the other hand, demonstrated progressive accumulation of fluorescent puncta in photoreceptors (Figs. 2B and S3B; see also arrows in the relative insets) beginning at 24 h post-treatment. Quantitative analysis restricted to photoreceptors revealed significantly elevated fluorescence already 48 h post-treatment (Fig. 2C), confirming mGCAP1-His uptake and accumulation. The same analysis conducted in the ganglion cell layer exhibited similar patterns (Fig. 2D), with peak signals at 48 h and 96 h post-treatment, suggesting *trans*-retinal protein mobility following initial uptake, as the orientation would favor ganglion cell internalization.

After demonstrating retinal mGCAP1-His uptake and fluorescence increase over time (Fig. 2B, insets, and Fig. S3), we performed subcellular localization studies 24 h post-treatment employing co-immunostaining with cell-type-specific markers (Figs. 3 and S4) in order to investigate the localization of mGCAP1-His within the cells of the different layers. In particular, in photoreceptors mGCAP1-His (red) colocalized with the rod-specific rhodopsin kinase (GRK1, green), as visible by yellow puncta (Figs. 3A and S4A and arrows therein). Moreover, in ganglion cells, we detected mGCAP1-His in the cytosol (red signal) using phalloidin as plasma membrane marker (green signal) (Figs. 3B and S4B). The orthogonal sectioning analysis performed on the GCL (Fig. 3C) further demonstrated that the protein was inside the cells by all 3 dimensions (XY, XZ and YZ).

To assess the impact of the treatment on tissue integrity, we analyzed GFAP staining. A comparison between control explants (Fig. S5A) and treated explants (Fig. S5B) revealed no apparent differences in GFAP distribution, apart from changes consistent with physiological aging of the explants. In line with these observations, quantitative image analysis (Fig. S5C) showed no significant differences, indicating that the treatment does not induce tissue damage or accelerate aging.

Overall, these findings demonstrate successful spontaneous internalization of recombinant protein following single-dose administration to retinal explants. The protein accumulated in both photoreceptors (the physiological site of action) and ganglion cells (whose axons comprise the optic nerve), suggesting potential therapeutic applications for both outer and inner retinal pathologies.

3.3. *Porcine retina explants as a model for testing the delivery to cone-rich regions*

We demonstrated that, in murine retinas, the delivered retina-specific protein mGCAP1-His, undergoes spontaneous cellular internalization, exhibits accumulation in both inner retinal layers and the outer photoreceptor compartment (rods), and does not compromise tissue viability. Nevertheless, the rod-dominated architecture of murine retina – where cones constitute less than 3% of the total photoreceptor population (Jeon et al., 1998) – presents a significant translational limitation, given that cone photoreceptors are predominantly affected in most severe inherited retinal degenerations (IRDs). To address this constraint, we transitioned to a more clinically relevant model utilizing porcine retinal explants. Porcine retinal tissue offers distinct experimental advantages: i) anatomical similarity to human retinal architecture, including a visual streak that closely resembles the human macula; ii) extended viability in *ex vivo* culture conditions (Weller et al., 2024); and iii) further ethical compliance with the 3Rs principle employing ocular tissue sourced as food industry byproducts, thereby eliminating the need for dedicated animal sacrifice.

To establish baseline conditions, we initially replicated the murine treatment protocol with increased protein concentrations to improve visualization of biodistribution. Differently from the murine studies, both myristoylated (mGCAP1-His) and non-myristoylated (nmGCAP1-His) protein variants were administered to evaluate whether the N-terminal fatty acid modification influences cellular uptake kinetics, potentially through enhanced membrane interactions. Temporal analysis was conducted at two critical time points—1 day and 7 days post-treatment—with comprehensive results presented in Figs. 4 and S6.

Control explants (Fig. 4A, B) exhibited characteristic aging-related changes over the experimental timeframe. At 24 h, retinal laminar organization remained well-preserved, with cone photoreceptors maintaining their typical morphological features (Fig. 4A, inset). However, by day 7 (Fig. 4B), several degenerative markers became evident: i) disrupted chromatin condensation patterns within both outer nuclear layer (ONL) and inner nuclear layer (INL), as indicated by altered DAPI staining and aberrant anti-His reactivity in the INL; ii) emergence of green autofluorescence (Fig. 4B arrows)—a hallmark of inflammatory processes —prominently localized to ganglion cell somata and INL components; and iii) progressive cone photoreceptor degeneration. Importantly, porcine explants demonstrated distinct staining characteristics compared to murine tissue, showing less pronounced anti-His

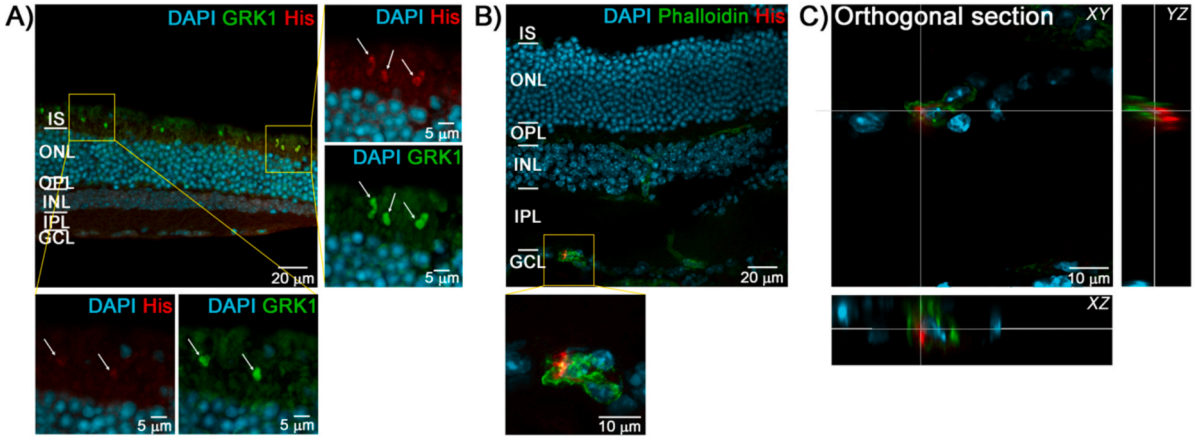

Fig. 3. mGCAP1-His localization in adult mouse retinal explants 24 h after-administration. A) Colocalization of mGCAP1-His with GRK1 in photoreceptors. Cryosections were processed as described in Methods. Images were acquired using a 20× air objective (0.8 NA) with a further 3× digital zoom (final magnification 60×). B) Explant section immunostained with anti–His antibody (red), counterstained with DAPI (cyan) and phalloidin-647 (green). Images were acquired with a 60× oil immersion objective (1.4 NA) while the inset has a final magnification of 180×. C) Orthogonal projection from B's inset illustrating the localization of the red signal within the cell, surrounded by green signal (plasma membrane) in all dimensions (*XY, XZ and YZ*). Panels A and B show optical sections corresponding to the maximum intensity signal across all channels. Additional z-stack projections are available upon request.

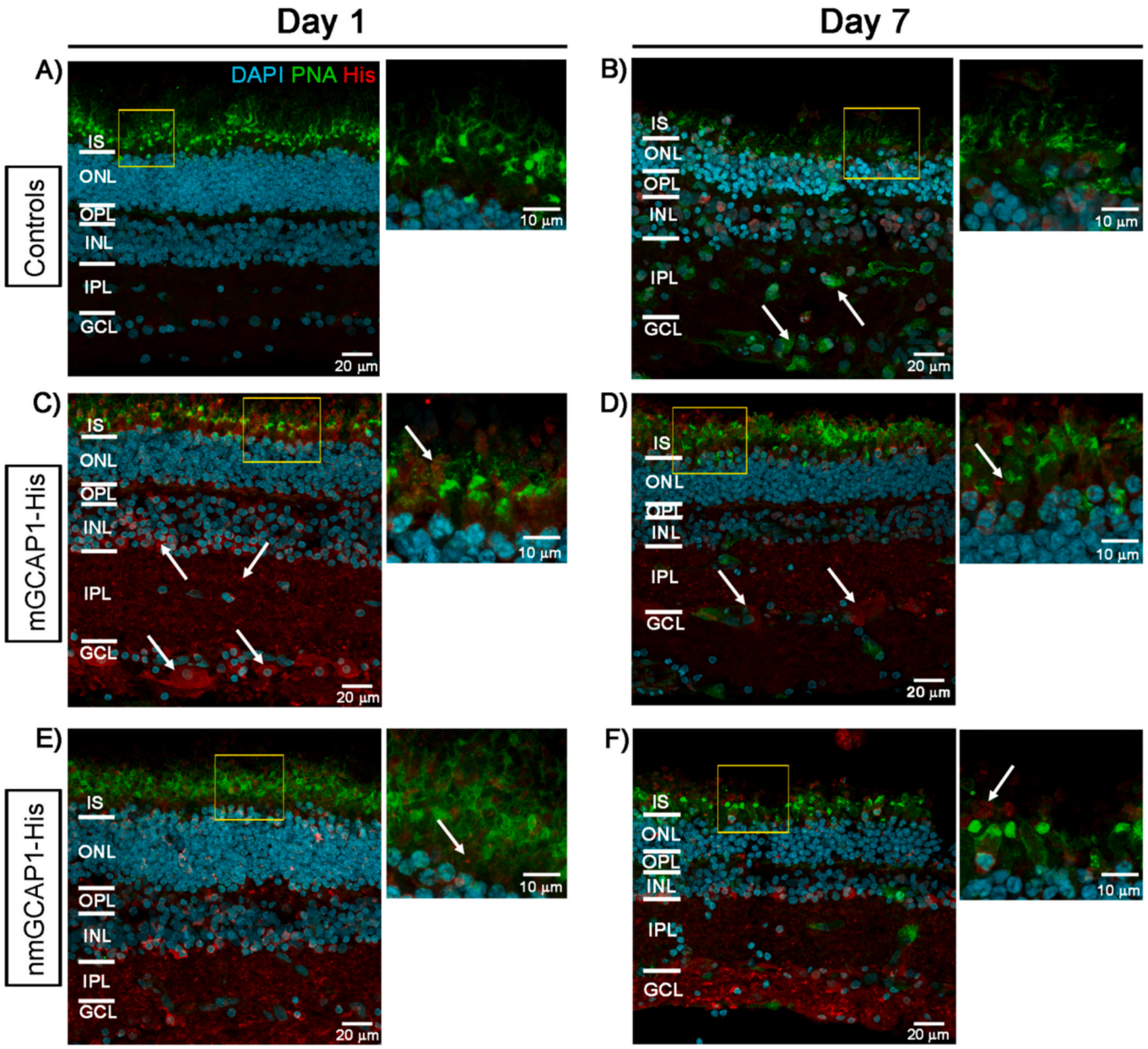

Fig. 4. Biodistribution of mGCAP1-His and nmGCAP1-His administrated as free proteins in pig retinal explants. A–B) Pig explants maintained in culture for 1 day (A) or 7 days (B) without treatment. C, D) Explants treated using ~44 µg mGCAP1-His and harvested after 1 day (C) or 7 days (D). E, F) Explants treated with ~44 µg nmGCAP1-His and collected after 1 day (E) or 7 days (F). Tissues were immunostained with PNA (green), anti–His-tag primary antibody (red) and nuclei were counterstained with DAPI (cyan). Images correspond to optical section with maximum detected signal. Acquisition was performed with a 60× oil immersion objective and an additional 2.3× digital zoom (final magnification 138× for insets).

immunostaining in specific retinal layers and exhibiting positive signals only under aging-related conditions.

Following mGCAP1-His administration, robust anti-His immunostaining was observed across all retinal layers within 24 h (Fig. 4C). Critically, the absence of direct colocalization with peanut agglutinin (PNA), despite spatial proximity (Fig. 4C, inset), demonstrated successful protein diffusion into cone photoreceptors. Additional immunolocalization patterns included distinct cytosolic distribution within ganglion cells, punctate labeling throughout the inner plexiform layer (IPL), and positive cellular profiles within the inner nuclear layer (INL) (see arrows in Fig. 4C). By day 7 (Fig. 4D), overall signal intensity had diminished yet remained detectable in the ganglion cell layer and in cone photoreceptors (Fig. 4D). In contrast, nmGCAP1-His treatment resulted in positive cones (Fig. 4E, inset) and ganglion cells labeling at 24 h, with preferential signal accumulation in the IPL–GCL region by day 7 (Fig. 4F). Collectively, these findings demonstrate that myristoylation does not modulate initial protein uptake efficiency but rather governs intracellular trafficking patterns and tissue biodistribution. Specifically, while both mGCAP1-His and nmGCAP1-His successfully enter retinal cells, the myristoyl modification appears to facilitate appropriate subcellular targeting, enabling sustained mGCAP1-His retention in both cone photoreceptors and ganglion cells.

To further investigate the tissue's apparent capacity to distinguish between retina-specific and foreign proteins, we examined the biodistribution of a non-retina-specific protein (mCar2-His). As shown in Fig. 1A, recombinant mCar2-His exhibits pronounced intrinsic fluorescence with peak excitation at approximately 600 nm. Given that fluorescence emission is critically dependent on protein structural integrity, we initially evaluated whether standard histological processing—including formalin fixation and detergent treatment—might

compromise fluorescence detection. Representative image acquired at 24 h using 594 nm laser excitation (Fig. S7A) revealed red fluorescent puncta predominantly localized to inner retinal regions, suggesting reduced photoreceptor accessibility compared to mGCAP1-His. To exclude potential processing artifacts, we conducted spectrofluorometric analysis of mCar2-His in phosphate-buffered saline versus 10% formalin under conditions mimicking confocal microscopy parameters (597 nm excitation). While spectral characteristics showed minimal solvent-dependent variations (Fig. S7B), significant fluorescence quenching was observed in formalin solutions. Considering the environmental sensitivity of mCar2-His—as validated by *in vitro* experiments and the differences relative to data obtained by immunofluorescence detection, we adopted His-tag-based protein tracking to ensure enhanced sensitivity and direct comparability with m/nmGCAP1-His results.

At 24 h post-administration, mCar2-His immunostaining was detected throughout all retinal layers (Figs. 5C and S8) compared to controls (Fig. 5A), with prominent signals at the inner limiting membrane, within ganglion cell somata, and in photoreceptor compartments (Fig. 5C arrows). However, signal intensity was reduced in OS compared to mGCAP1-His (Fig. 4C), despite employing identical detection protocols and administering essentially the same amount of protein (60 μg

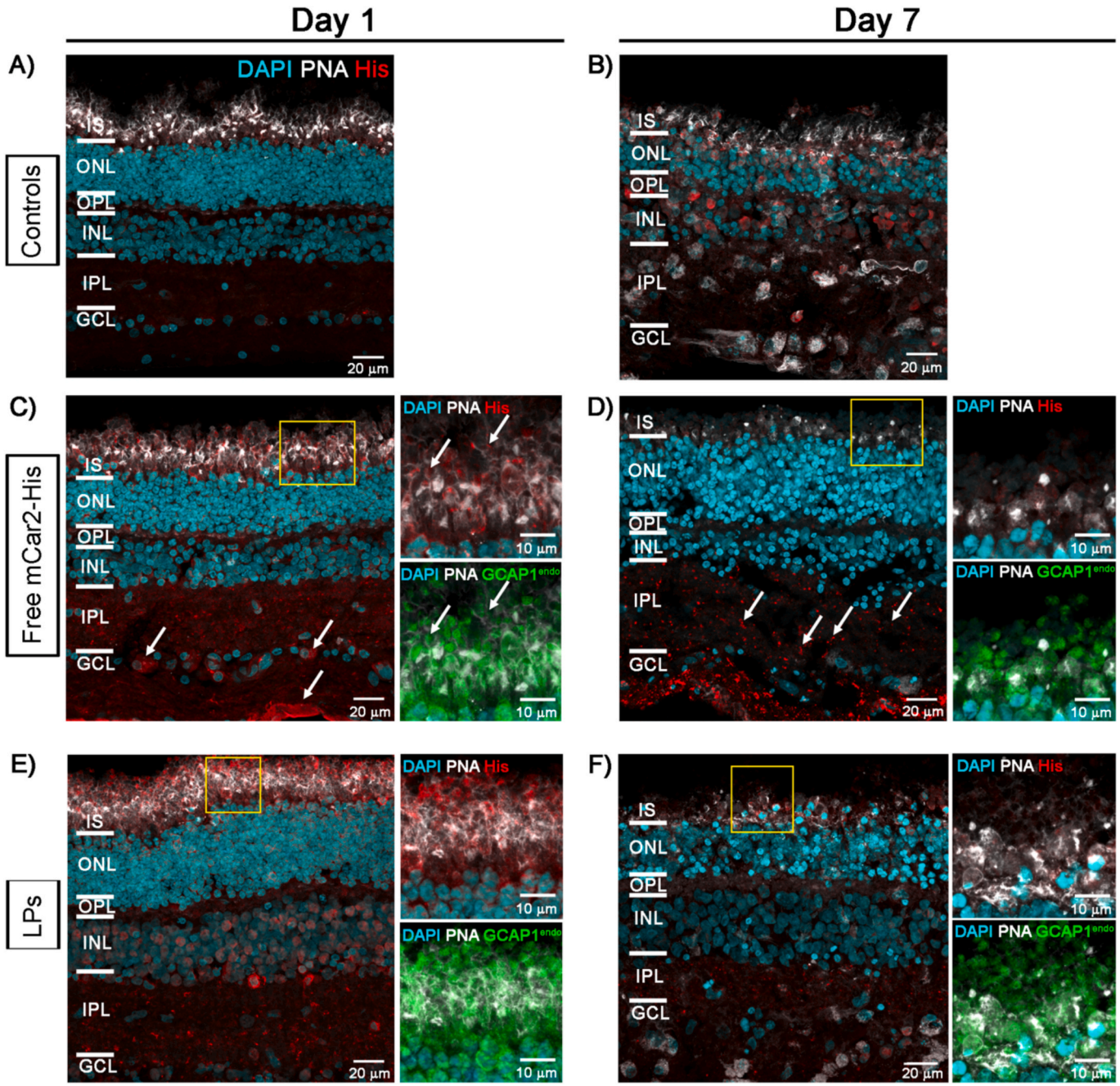

Fig. 5. Biodistribution of mCar2-His administrated as free protein or incapsulated into ROS-like liposomes in pig retinal explants. A–B) Pig explants maintained in culture for one day (A) or seven days (B) without treatment (same controls shown in Fig. 4). C–D) Explants treated with ~60 μg mCar2-His and collected after one day (C) or seven days (D). E–F) Explants treated with ROS-like liposomes loaded with mCar2-His and harvested after one day (E) or seven days (F). The administration volume was adjusted to deliver the same amount of protein as in the free form. Tissues were immunostained using PNA (white), anti–His-tag (red) and anti–endogenous GCAP1 antibodies (green). Nuclei were counterstained with DAPI (cyan). Images show optical sections with maximal signal intensity. Acquisition was performed using a 60× oil immersion objective with an additional 2.3× digital zoom (final magnification 138× for insets).

versus 44 μg, corresponding to 1.9 nmol in both conditions). Detailed examination of cone photoreceptors (Fig. 5C inset) revealed two distinct signal distributions: punctual and bright signal close to the membrane, suggesting a localization within closed intracellular compartments, and diffuse mCar2-His labeling (red) colocalizing with endogenous GCAP1 (green), consistent with successful internalization. This evidence is further supported by the orthogonal projections reported in Fig. S9A–C.

By day 7 (Fig. 5D), mCar2-His signal persisted within cone photoreceptors but exhibited reduced intensity compared to mGCAP1-His (Fig. 4D) and became predominantly restricted to inner retinal layers. These observations support the hypothesis that retinal tissue demonstrates preferential retention of retina-specific proteins (mGCAP1-His) over partially modified (nmGCAP1-His) or completely foreign proteins (mCar2-His).

To determine whether non-retina-specific protein uptake could be enhanced by a drug delivery system, we encapsulated mCar2-His in liposomes with a phospholipid composition designed to recapitulate photoreceptor disc membrane composition. This biomimetic delivery strategy aimed at enhancing cellular internalization by concealing foreign protein characteristics while leveraging endogenous mechanisms for liposome uptake. At 24 h post-treatment, encapsulated mCar2-His generated significantly enhanced signals (Fig. 5E inset) compared to free protein administration (Fig. 5C inset). Deconvoluted imaging analysis following co-staining of GCAP1 (green) and mCar2-His (red) (Fig. S9D–E) corroborated improved protein delivery efficiency, as evidenced by increased yellowish fluorescent spots within outer segment interiors, clearly visualized through orthogonal sectioning (XY, XZ, and YZ planes) (Fig. S5E). Nevertheless, by day 7, cone-associated signals from encapsulated mCar2-His (Fig. 5F) had declined to control levels (Fig. 5B), suggesting that retinal tissue may adopt faster clearance of non-retina-specific proteins regardless of delivery methodology.

4. Discussion

This study presents a robust and accessible experimental framework for testing protein delivery to both inner and outer retinal layers. The experimental model we propose aligns with the 3Rs principle by reducing the number of mice required through the use of retinal quarters rather than whole retinas, and by utilizing porcine retinas derived from food industry byproducts, with the additional advantage of extending delivery studies to cone-rich regions that mimic the human macula. Furthermore, we have demonstrated that the proposed treatments are not detrimental to cellular viability in both animal models under pharmacologically relevant conditions.

Our data clearly demonstrate that delivered proteins enter retinal neurons and accumulate in both photoreceptor and ganglion cell layers, with a distinct preference for retina-specific proteins in their most native configuration—specifically, those bearing post-translational modifications such as myristoylation, which are essential for proper biological function. These findings have considerable translational relevance and important therapeutic implications for the treatment of IRDs, particularly those of autosomal dominant inheritance. Additionally, non-retina-specific proteins, such as mCar2-His, can be effectively delivered to the retina following encapsulation in biocompatible liposomes; however, their persistence in porcine retinal tissue remains inferior compared to native counterparts. This observation, together with the differential biodistribution patterns observed when comparing mGCAP1-His with nmGCAP1-His delivery, suggests the existence of protein-specific proteostasis mechanisms that warrant detailed investigation in future studies. Our data suggest that retinal tissue possesses sophisticated mechanisms for discriminating between retina-specific and non-specific proteins, as evidenced by the preferential uptake and retention of mGCAP1-His compared to mCar2-His. This selectivity may involve specific cellular recognition pathways yet to be elucidated, which facilitate internalization of proteins bearing appropriate structural signatures. The physicochemical properties of a drug molecule, including size, charge, and hydrophilicity, drastically affect the efficacy of administration, and our results support this concept by demonstrating that myristoylation significantly influences intracellular trafficking patterns for GCAP1. Indeed, the observed differential biodistribution between myristoylated and non-myristoylated GCAP1 variants aligns with established principles of protein trafficking, suggesting that retinal tissue possesses specific recognition mechanisms for properly modified endogenous proteins (Lopez-Begines et al., 2018; Peshenko et al., 2012).

Several promising avenues emerge from our findings. Mechanistic studies aimed at elucidating the molecular basis of protein-selective uptake could inform the design of optimized therapeutics with enhanced bioavailability and specificity for intraocular delivery (Shastri et al., 2023). Additionally, expansion of our protein repertoire to include other therapeutically relevant targets, such as neurotrophic factors or genome editing systems, could broaden the therapeutic applications of our platform (Boddu et al., 2023). While the translation of our *ex vivo* findings to *in vivo* models will be essential for advancing protein delivery approaches toward clinical implementation, our protein delivery model could serve as a valuable tool for rapid therapeutic screening and dose optimization prior to more invasive interventions.

5. Conclusions

This study establishes a robust *ex vivo* platform for evaluating protein delivery to both peripheral and macular retinal regions, providing a translational framework that bridges basic research and clinical application. Using murine and porcine retinal explants, we demonstrated spontaneous internalization and sustained accumulation of therapeutic proteins in photoreceptors and ganglion cells following single-dose administration. Key findings include: i) successful delivery of retina-specific proteins (GCAP1) to their physiological targets with appropriate subcellular localization in rod and cone photoreceptors over extended culture periods without inducing tissue damage; ii) differential biodistribution governed by post-translational modifications, with myristoylated variants exhibiting superior retention and proper trafficking compared to non-modified forms; iii) suggestion of sophisticated protein-selective recognition mechanisms, whereby retinal tissue preferentially retains native proteins over foreign ones; and iv) enhanced initial uptake of non-retina-specific proteins through liposomal encapsulation, though long-term retention remained inferior to native counterparts. These observations establish our *ex vivo* system as a valuable screening tool for optimizing protein therapeutics and delivery formulations, while simultaneously providing mechanistic insights into protein-selective cellular uptake. The dual targeting capability—demonstrating accumulation in both outer retinal layers (photoreceptors) and inner retinal structures (ganglion cells)—positions this approach for treating a broad spectrum of retinal diseases, including inherited retinal dystrophies, age-related macular degeneration, glaucoma, and optic neuropathies. Future studies should focus on elucidating the molecular mechanisms underlying protein-selective uptake, expanding the therapeutic protein repertoire to include neurotrophic factors and genome editing systems, and validating these findings in *in vivo* models to advance toward clinical translation.

6. Funding sources

This study was supported by a grant from the Velux Stiftung (Project No. 1410) and by the Next Generation EU/Ministry of University and Research project: “A multiscale integrated approach to the study of the nervous system in health and disease (MNESYS)”, CUP B33C22001060002, PE00000006 missione 4, componente 2, investimento 1.3. The kind support of Retina Italia OdV is gratefully acknowledged. Giuditta Dal Cortivo was the recipient of an EMBO Scientific Exchange Grant Number 9340.

CRediT authorship contribution statement

Giuditta Dal Cortivo: Writing – review & editing, Writing – original draft, Methodology, Investigation, Formal analysis, Conceptualization. **Carmen Longo:** Writing – review & editing, Writing – original draft, Methodology, Investigation. **Brigitte Müller:** Supervision, Methodology. **Anna Avesani:** Investigation. **Raffaella Pacchiana:** Formal analysis. **Maria Weller:** Methodology. **Valerio Marino:** Writing – review & editing, Writing – original draft, Investigation. **Lyubomyr Lytvynchuk:** Writing – review & editing, Conceptualization. **Knut Stieger:** Writing – review & editing, Validation, Supervision, Resources, Conceptualization. **Daniele Dell'Orco:** Writing – review & editing, Writing – original draft, Validation, Supervision, Resources, Project administration, Funding acquisition, Conceptualization.

Declaration of competing interest

The authors declare that they have no known competing financial interests or personal relationships that could have appeared to influence the work reported in this paper.

Acknowledgments

The Centro Piattaforme Tecnologiche of the University of Verona is acknowledged for providing access to the Imaging and Spectroscopy, diffractometry and molecular interaction study platform. The authors wish to thank Dr Jeannie Chen for kindly providing primary anti-GCAP1 antibodies.

Appendix A. Supplementary data

Supplementary data to this article can be found online at https://doi.org/10.1016/j.ijpharm.2026.126568.

Data availability

Data will be made available on request.

References

Abbas, S., Marino, V., Weisschuh, N., Kieninger, S., Solaki, M., Dell'Orco, D., Koch, K.W., 2020. Neuronal calcium sensor GCAP1 encoded by GUCA1A exhibits heterogeneous functional properties in two cases of retinitis pigmentosa. ACS Chem. Nerosci. 11, 1458–1470.

Asteriti, S., Dal Cortivo, G., Pontelli, V., Cangiano, L., Buffelli, M., Dell'Orco, D., 2015. Effective delivery of recombinant proteins to rod photoreceptors via lipid nanovesicles. Biochem. Biophys. Res. Commun. 461, 665–670.

Asteriti, S., Marino, V., Avesani, A., Biasi, A., Dal Cortivo, G., Cangiano, L., Dell'Orco, D., 2023. Recombinant protein delivery enables modulation of the phototransduction cascade in mouse retina. Cell. Mol. Life Sci. 80, 371.

Attia, S.A., MacKay, J.A., 2022. Protein and polypeptide mediated delivery to the eye. Adv. Drug Deliv. Rev. 188, 114441.

Biasi, A., Marino, V., Dal Cortivo, G., Maltese, P.E., Modarelli, A.M., Bertelli, M., Colombo, L., Dell'Orco, D., 2021. A novel GUCA1A variant associated with cone dystrophy alters cGMP signaling in photoreceptors by strongly interacting with and hyperactivating retinal guanylate cyclase. Int. J. Mol. Sci. 22.

Boddu, S.H.S., Acharya, D., Hala, V., Jani, H., Pande, S., Patel, C., Shahwan, M., Jwala, R., Ranch, K.M., 2023. An update on strategies to deliver protein and peptide drugs to the eye. ACS Omega 8, 35470–35498.

Chilumuri, A., Markiv, A., Milton, N.G., 2014. Immunocytochemical staining of endogenous nuclear proteins with the HIS-1 anti-poly-histidine monoclonal antibody: a potential source of error in His-tagged protein detection. Acta Histochem. 116, 1022–1028.

Dal Cortivo, G., Marino, V., Boni, F., Milani, M., Dell'Orco, D., 2020. Missense mutations affecting Ca(2+)-coordination in GCAP1 lead to cone-rod dystrophies by altering protein structural and functional properties. Biochim. Biophys. Acta 1867, 118794.

Dell'Orco, D., Behnen, P., Linse, S., Koch, K.W., 2010. Calcium binding, structural stability and guanylate cyclase activation in GCAP1 variants associated with human cone dystrophy. Cell. Mol. Life Sci. 67, 973–984.

Dizhoor, A.M., Boikov, S.G., Olshevskaya, E.V., 1998. Constitutive activation of photoreceptor guanylate cyclase by Y99C mutant of GCAP-1. Possible role in causing human autosomal dominant cone degeneration. J. Biol. Chem. 273, 17311–17314.

El Sanharawi, M., Kowalczuk, L., Touchard, E., Omri, S., de Kozak, Y., Behar-Cohen, F., 2010. Protein delivery for retinal diseases: from basic considerations to clinical applications. Prog. Retin. Eye Res. 29, 443–465.

Fu, Y., Yau, K.W., 2007. Phototransduction in mouse rods and cones. Pflugers Arch. 454, 805–819.

Hanany, M., Shalom, S., Ben-Yosef, T., Sharon, D., 2024. Comparison of worldwide disease prevalence and genetic prevalence of inherited retinal diseases and variant interpretation considerations. Cold Spring Harb. Perspect. Med. 14.

Hwang, J.Y., Koch, K.W., 2002. Calcium- and myristoyl-dependent properties of guanylate cyclase-activating protein-1 and protein-2. Biochemistry 41, 13021–13028.

Hwang, J.Y., Lange, C., Helten, A., Hoppner-Heitmann, D., Duda, T., Sharma, R.K., Koch, K.W., 2003. Regulatory modes of rod outer segment membrane guanylate cyclase differ in catalytic efficiency and Ca(2+)-sensitivity. Eur. J. Biochem. 270, 3814–3821.

Jeon, C.J., Strettoi, E., Masland, R.H., 1998. The major cell populations of the mouse retina. J. Neurosci. 18, 8936–8946.

Jiang, L., Wheaton, D., Bereta, G., Zhang, K., Palczewski, K., Birch, D.G., Baehr, W., 2008. A novel GCAP1(N104K) mutation in EF-hand 3 (EF3) linked to autosomal dominant cone dystrophy. Vision Res. 48, 2425–2432.

Kamenarova, K., Corton, M., Garcia-Sandoval, B., Fernandez-San Jose, P., Panchev, V., Avila-Fernandez, A., Lopez-Molina, M.I., Chakarova, C., Ayuso, C., Bhattacharya, S. S., 2013. Novel GUCA1A mutations suggesting possible mechanisms of pathogenesis in cone, cone-rod, and macular dystrophy patients. Biomed Res. Int. 2013, 517570.

Karp, H., Zoltek, M., Wasko, K., Vazquez, A.L., Brim, J., Ngo, W., Schepartz, A., Doudna, J.A., 2025. Packaged delivery of CRISPR-Cas9 ribonucleoproteins accelerates genome editing. Nucleic Acids Res. 53.

Kim, T.Y., Yoon, T.S., Kang, S., Afzal, M., 2022. Juggling with fluorescent proteins: Spectrum and structural changes of the mCardinal2 variants. Biochem. Biophys. Res. Commun. 593, 79–83.

Kitiratschky, V.B., Behnen, P., Kellner, U., Heckenlively, J.R., Zrenner, E., Jagle, H., Kohl, S., Wissinger, B., Koch, K.W., 2009. Mutations in the GUCA1A gene involved in hereditary cone dystrophies impair calcium-mediated regulation of guanylate cyclase. Hum. Mutat. 30, E782–E796.

Koch, K.W., Dell'orco, D., 2013. A calcium-relay mechanism in vertebrate phototransduction. ACS Chem. Nerosci. 4, 909–917.

Koch, K.W., Dell'Orco, D., 2015. Protein and signaling networks in vertebrate photoreceptor cells. Front. Mol. Neurosci. 8, 67.

Lopez-Begines, S., Plana-Bonamaiso, A., Mendez, A., 2018. Molecular determinants of guanylate cyclase activating protein subcellular distribution in photoreceptor cells of the retina. Sci. Rep. 8, 2903.

Mandal, A., Pal, D., Agrahari, V., Trinh, H.M., Joseph, M., Mitra, A.K., 2018. Ocular delivery of proteins and peptides: challenges and novel formulation approaches. Adv. Drug Deliv. Rev. 126, 67–95.

Manes, G., Mamouni, S., Herald, E., Richard, A.C., Senechal, A., Aouad, K., Bocquet, B., Meunier, I., Hamel, C.P., 2017. Cone dystrophy or macular dystrophy associated with novel autosomal dominant GUCA1A mutations. Mol. Vis. 23, 198–209.

Marino, V., Dal Cortivo, G., Maltese, P.E., Placidi, G., De Siena, E., Falsini, B., Bertelli, M., Dell'Orco, D., 2021. Impaired Ca(2+) sensitivity of a novel GCAP1 variant causes cone dystrophy and leads to abnormal synaptic transmission between photoreceptors and bipolar cells. Int. J. Mol. Sci. 22.

Marino, V., Dal Cortivo, G., Oppici, E., Maltese, P.E., D'Esposito, F., Manara, E., Ziccardi, L., Falsini, B., Magli, A., Bertelli, M., Dell'Orco, D., 2018. A novel p.(Glu111Val) missense mutation in GUCA1A associated with cone-rod dystrophy leads to impaired calcium sensing and perturbed second messenger homeostasis in photoreceptors. Hum. Mol. Genet. 27, 4204–4217.

Marino, V., Sulmann, S., Koch, K.W., Dell'Orco, D., 2015. Structural effects of Mg(2)(+) on the regulatory states of three neuronal calcium sensors operating in vertebrate phototransduction. BBA 1853, 2055–2065.

Muller, B., 2019. Organotypic culture of adult mouse retina. Methods Mol. Biol. 1940, 181–191.

Muller, B., Wagner, F., Lorenz, B., Stieger, K., 2017. Organotypic cultures of adult mouse retina: morphologic changes and gene expression. Invest. Ophthalmol. Vis. Sci. 58, 1930–1940.

Nishiguchi, K.M., Sokal, I., Yang, L., Roychowdhury, N., Palczewski, K., Berson, E.L., Dryja, T.P., Baehr, W., 2004. A novel mutation (I143NT) in guanylate cyclase-activating protein 1 (GCAP1) associated with autosomal dominant cone degeneration. Invest. Ophthalmol. Vis. Sci. 45, 3863–3870.

Peshenko, I.V., Cideciyan, A.V., Sumaroka, A., Olshevskaya, E.V., Scholten, A., Abbas, S., Koch, K.W., Jacobson, S.G., Dizhoor, A.M., 2019. A G86R mutation in the calcium-sensor protein GCAP1 alters regulation of retinal guanylyl cyclase and causes dominant cone-rod degeneration. J. Biol. Chem. 294, 3476–3488.

Peshenko, I.V., Olshevskaya, E.V., Dizhoor, A.M., 2012. Interaction of GCAP1 with retinal guanylyl cyclase and calcium: sensitivity to fatty acylation. Front. Mol. Neurosci. 5, 19.

Rosas-Arellano, A., Villalobos-Gonzalez, J.B., Palma-Tirado, L., Beltran, F.A., Carabez-Trejo, A., Missirlis, F., Castro, M.A., 2016. A simple solution for antibody signal enhancement in immunofluorescence and triple immunogold assays. Histochem. Cell Biol. 146, 421–430.

Shastri, D.H., Silva, A.C., Almeida, H., 2023. Ocular delivery of therapeutic proteins. A review. Pharmaceutics 15.

Singh, M., Negi, R., Alka, Vinayagam, R., Kang, S.G., Shukla, P., 2024. Age-related macular degeneration (AMD): pathophysiology, drug targeting approaches, and recent developments in nanotherapeutics. Medicina 60 (10), 1647.

Sokal, I., Dupps, W.J., Grassi, M.A., Brown Jr., J., Affatigato, L.M., Roychowdhury, N., Yang, L., Filipek, S., Palczewski, K., Stone, E.M., Baehr, W., 2005. A novel GCAP1

missense mutation (L151F) in a large family with autosomal dominant cone-rod dystrophy (adCORD). Invest. Ophthalmol. Vis. Sci. 46, 1124–1132.
Sokal, I., Li, N., Surgucheva, I., Warren, M.J., Payne, A.M., Bhattacharya, S.S., Baehr, W., Palczewski, K., 1998. GCAP1 (Y99C) mutant is constitutively active in autosomal dominant cone dystrophy. Mol. Cell 2, 129–133.
Tham, Y.C., Li, X., Wong, T.Y., Quigley, H.A., Aung, T., Cheng, C.Y., 2014. Global prevalence of glaucoma and projections of glaucoma burden through 2040: a systematic review and meta-analysis. Ophthalmology 121, 2081–2090.
Viviano, J., Krishnan, A., Wu, H., Venkataraman, V., 2016. Electrophoretic mobility shift in native gels indicates calcium-dependent structural changes of neuronal calcium sensor proteins. Anal. Biochem. 494, 93–100.
Vocke, F., Weisschuh, N., Marino, V., Malfatti, S., Jacobson, S.G., Reiff, C.M., Dell'Orco, D., Koch, K.W., 2017. Dysfunction of cGMP signalling in photoreceptors by a macular dystrophy-related mutation in the calcium sensor GCAP1. Hum. Mol. Genet. 26, 133–144.
Weller, M., Muller, B., Stieger, K., 2024. Long-term porcine retina explants as an alternative to in vivo experimentation. Transl. Vis. Sci. Technol. 13, 9.
Wilkie, S.E., Li, Y., Deery, E.C., Newbold, R.J., Garibaldi, D., Bateman, J.B., Zhang, H., Lin, W., Zack, D.J., Bhattacharya, S.S., Warren, M.J., Hunt, D.M., Zhang, K., 2001. Identification and functional consequences of a new mutation (E155G) in the gene for GCAP1 that causes autosomal dominant cone dystrophy. Am. J. Hum. Genet. 69, 471–480.
Wong, W.L., Su, X., Li, X., Cheung, C.M., Klein, R., Cheng, C.Y., Wong, T.Y., 2014. Global prevalence of age-related macular degeneration and disease burden projection for 2020 and 2040: a systematic review and meta-analysis. Lancet Glob. Health 2, e106–e116.